Magnetic Flux Topology of 2D Point Dipoles

Sven Bachthaler[1], Filip Sadlo[1], Rudolf Weeber[2], Sofia Kantorovich[2], Christian Holm[2], and Daniel Weiskopf[1]

[1]VISUS, University of Stuttgart, Germany
[2]Institute for Computational Physics, University of Stuttgart, Germany

Abstract
Magnetic fields exhibit higher-order, nonlinear singularities in the form of point-dipole singularities. In addition, due to absence of divergence, they feature only a subset of invariant structures from traditional vector field topology. For magnetic fields of sets of point dipoles—widely present in physics and often used as an approximation—we present a technique revealing the topology of magnetic flux. The flux topology is identified with areas covered by field lines that directly connect pairs of dipoles. We introduce the dipole connectrix as a reduced one-manifold representation of those areas. The set of connectrices serves as our concise visualization of the global structure of magnetic flux. In addition, the quantitative values of flux are displayed by the thickness of the connectrices. We evaluate our technique for simulations of ferroparticle monolayers and magnetic gels.

Categories and Subject Descriptors (according to ACM CCS): I.6.6 [Simulation and Modeling]: Simulation Output Analysis—; J.2 [Physical Sciences and Engineering]: Physics—

1. Introduction

Magnetic fields are a subclass of vector fields with some restrictions compared to generic vector fields. A magnetic field is divergence-free; therefore, its field lines are either closed or of infinite length. Inspired by traditional vector field topology, we want to visualize the topology of magnetic flux. However, established methods from vector field topology cannot be applied in a straightforward manner because the vector field (i.e., the magnetic flux density) may be infinite at singularity points. The most prominent example of such a singularity is the magnetic dipole, which is our central object of investigation.

In this paper, we focus on static 2D magnetic fields created by sets of dipoles. Since there are no magnetic monopoles, the first non-trivial term in any field expansion is represented by a dipole. Furthermore, elementary particles like electrons are points (without physical extent) that carry the magnetic moment of a dipole. Hence, the dipole representation is highly relevant for magnetic fields. One natural way of visualizing a magnetic field is to use field lines. Although field lines are directed and a magnetic flux is present, there is no transport of any matter involved per se. We are particularly interested in the global structure of the magnetic flux between dipoles, i.e., the connectivity of dipoles via magnetic field lines. We exploit the fact that the topology of magnetic fields is reduced to only two types of

critical points: dipoles and saddles. We will argue that magnetic flux through two dipoles is found in a region that is always bounded by two saddles. Although similar to Morse-Smale cells, these regions are also bounded by dipoles instead of sources and sinks. We utilize the interdependence of the magnetic field and its corresponding vector potential to locate these regions. Our main contribution is the definition of distinguished field lines that connect two dipoles and are used to visualize the topology of magnetic flux. We call this new topological construct *dipole connectrix*, or shorter connectrix. Given the task of finding dipoles that interact with each other, e.g., are forming rings or chains of magnetic flux, it is possible to use traditional topology. However, to accomplish this, the user has to keep track of several topological curves at once. By using connectrices, this task is reduced to following a single line. We refer to Fig. 1 for a comparison of traditional vector field topology and flux topology.

The contributions of our approach are (i) a concept that visualizes the topological structure of magnetic flux between dipoles, and (ii) a technique that provides a quantitative representation of magnetic flux.

As an application of our visualization technique, we present results from the simulation of systems of single domain magnetic nanoparticles. The simplest example of such a system to which our visualization has great potential is a magnetic fluid, consisting of magnetic particles with an aver-
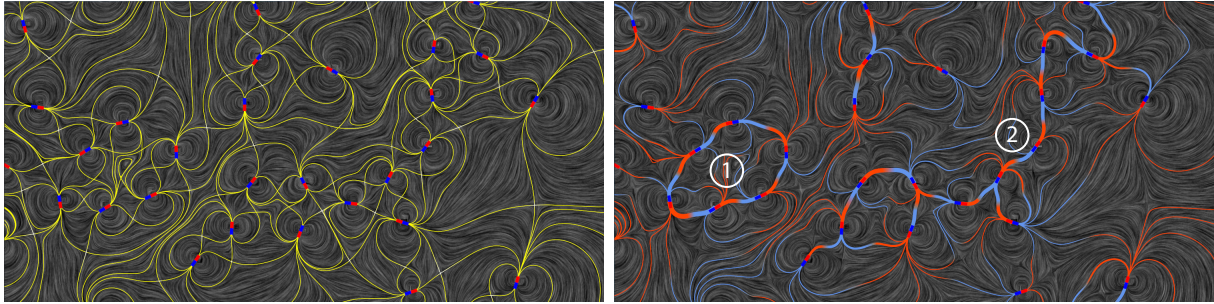
Figure 1: *Comparison of traditional topology (left) and flux topology (right). Dipoles are represented as a two-colored rectangles with a red north pole and a blue south pole. With flux topology, magnetic rings* (1) *or chains* (2) *are easier to identify.*

age size of 7–9 nm, suspended in a non-magnetic carrier liquid. Direct investigation of the 3D clustering process in these media is difficult. However, thin films of these fluids allow for experimental inspection with transmission electron microscopy and are in accordance with recent simulations. Recent experiments [KDK*06] have shown how complex the microstructure of 2D layers of a ferrofluid can be. Additional insight into these systems was obtained in theory and by computer simulation [KCH08], [PDKH09]. However, none of these approaches can directly characterize the field distribution in the sample.

Another approach blends magnetic and elastic properties within a single material, by embedding magnetic nanoparticles into an elastic polymer matrix. Materials that are designed as such are called magnetic gels, or ferrogels, and can serve as the basis for various potential applications, ranging from artificial muscles, actuators, and micromachines to biomimetic energy-transducing devices. A manifestation of magneto-elastic coupling can be observed in the deformation of a macroscopic ferrogel body in a uniform or gradient magnetic field [Zri00], [RDT*10]. However, any application of these materials is based on the profound knowledge of their microstructure and on the ability to control and design them on various levels. There are only few theories that can treat the gel on the mesoscopic level, see the work [SRB11] and references there in, and simulations [WC11] aimed at the understanding of the gel microstructure. Therefore, any additional knowledge of the magnetic field is of high relevance for further development of theoretical models.

2. Related Work

In this work, we focus on magnetostatic fields, which we treat as vector fields from a visualization point of view. Other works that specifically address the visualization of magnetic fields are for example the paper of Sundquist [Sun03], which introduces dynamic line integral convolution to visualize electromagnetic fields. Klein et al. [KE04] present an approach that uses a discrete particle model to visualize magnetic field lines. Thomaszewski et al. [TGPS08] focus on the simulation part, introducing magnetic interaction for

rigid body simulations with individual dipoles. However, the visualization of fields is not the main aspect of their work. Sadlo et al. adopt magnetic field visualization to vorticity in vortical flow [SPP04], [SPS06]. In contrast to our work, all of the above papers ignore the topology of vector fields.

The majority of topological methods for vector field analysis can be categorized in two groups: those that focus on regions of qualitatively similar behavior, and those that are dual to this approach—being concerned with the lower-dimensional constructs separating these regions. A prominent example of the former one is Morse-Smale decomposition [GBHP08], whereas separatrix-based topologies account to the latter. An extensive survey of topology-based methods in flow visualization is provided by Laramee et al. [LHZP07].

Topology—a theory of connectivity—is primarily known for its utility in the study of (geometric) manifolds in mathematics and physics. Interestingly, this concept can be transferred to initial value problems in dynamical system theory and vector fields. Vector field topology aims at revealing the essential structure by means of distinguished trajectories—providing insight in "connectivity due to transport". We closely follow this argumentation by focusing on "connectivity due to magnetic flux".

In visualization, vector field topology was introduced by Helman and Hesselink for 2D [HH89] and 3D [HH91] vector fields. The visualization of the topology of the subset of *magnetic* vector fields is presented, e.g., by Sanderson et al. [SCT*10], [SCTC11], who provide techniques that visualize the topology of magnetic fields in the context of fusion reactors. They, however, are interested in "islands of stability" in a chaotic field [PS07], [PS09]—they do not visualize magnetic flux. Another example is the work of Cai et al. [CLN05], who apply traditional vector field topology to magnetic fields.

Probably closest related to our work is the extraction of higher-order singularities from 2D vector fields by Scheuermann et al. [SHK*97]. There is, however, the major difference that the magnitude of our magnetic vector field be-

comes infinite at the dipoles with flux going through their center, whereas Scheuermann et al. address higher-order critical points, i.e., stationary points of a continuous vector field that vanishes at those points.

Since divergence-free fields exhibit closed field lines, a related concept in traditional vector field topology is the one of periodic orbits. However, field lines in divergence-free vector fields are either closed or reach a boundary; therefore, extracting these structures would not provide insightful visualizations in our case. Furthermore, periodic orbits would have to be isolated in classical vector field topology to represent an invariant structure, e.g., as shown by Wischgoll and Scheuermann [WS01], who extract closed streamlines from planar vector fields.

In our work, we rely on a dual-topology approach employing not only the magnetic field but also the gradient of its vector potential. Rosanwo et al. [RPP*09] use a dual-topology approach to perform streamline placement. Similar to the gradient field of our vector potential, their dual field is orthogonal to the visualized vector field. Another example of an approach that exploits the duality of vector fields is the work of Bachthaler and Weiskopf [BW08], where line patterns perpendicular to the underlying vector field visualize the motion of the flow field.

Physically related, but not of immediate algorithmic interest to us is the area of electric fields. Here, Andrae et al. [ABB*11] and Barth et al. [BHI*09] present techniques that compute and visualize electronic flux. A survey of visualization methods for physical sciences is provided by Lipşa et al. [LLC*11].

3. Dual Topology of Magnetic Fields

In this section, we first summarize the physical background that we need in this paper. We then advance to our formulation of dual vector field topology for the class of vector fields in which we are interested. This dual vector field is the basis for our flux topology introduced in Sect. 4.

3.1. Physics of Magnetostatics

We briefly review the physics of magnetostatics, as far as it is relevant for this paper. We refer to the textbook by Jackson [Jac75] for a comprehensive introduction to magnetostatics in particular, and classical electrodynamics in general. We assume the setting of magnetostatics, i.e., we ignore any magnetic effects that may be additionally introduced from dynamics. Such a scenario is relevant for typical setups with steady-state behavior.

The key observation is that there are no magnetic monopoles (in contrast to electrostatics with its electric monopole). Therefore, magnetic dipoles serve as the main building blocks for establishing magnetic fields. A single dipole is described by its *magnetic moment*

$$\mathbf{m} = \frac{1}{2c} \int \mathbf{x} \times \mathbf{J}(\mathbf{x}) \, d^3 x \qquad (1)$$

located at position $\mathbf{x}$ with the *current distribution* $\mathbf{J}$ and the speed of light c.

It is common practice to use the *vector potential* $\mathbf{A}$ to describe the magnetic field. The term "magnetic field" itself is often used to refer to the *magnetic flux density* $\mathbf{B}$, which is related to $\mathbf{A}$ as follows:

$$\mathbf{B} = \text{curl } \mathbf{A}.$$

Therefore, magnetism may be described using $\mathbf{A}$ or $\mathbf{B}$. In fact, many computations in physics are based on the vector potential. In particular, computations often use series expansions of the vector potential, similar to Taylor expansions of functions. The mathematical background is based on the expansion by vector spherical harmonics [Jac75]. This kind of expansion reads for the i-th component of $\mathbf{A}$:

$$A_i(\mathbf{x}) = \frac{1}{c||\mathbf{x}||} \int J_i(\mathbf{x}') \, d^3 x' + \frac{1}{c||\mathbf{x}||^3} \int J_i(\mathbf{x}') \mathbf{x}' \, d^3 x' + \cdots$$

Here, $\mathbf{J}$ is the current distribution that gives rise to the magnetic field. If only the first term of the expansion is used, we obtain

$$\mathbf{A}(\mathbf{x}) = \frac{\mathbf{m} \times \mathbf{x}}{||\mathbf{x}||^3}$$

where $\mathbf{m}$ is the magnetic moment of a magnetic dipole (Eq. (1)). Put differently, the expansion of $\mathbf{A}$ up to the first nonvanishing term yields a magnetic dipole. Therefore, dipoles are highly relevant as, at least approximative, representation of any magnetic field; the more localized the current distribution, the better the approximation.

Finally, the magnetic flux density corresponding to $\mathbf{A}$ of the magnetic dipole reads:

$$\mathbf{B}(\mathbf{x}) = \frac{3\mathbf{n}(\mathbf{n} \cdot \mathbf{m}) - \mathbf{m}}{||\mathbf{x}||^3}$$

where $\mathbf{n} = \frac{\mathbf{x}}{||\mathbf{x}||}$.

3.2. Dual Vector Field Topology

To describe the flux topology of 2D magnetic fields, we first reformulate the 3D vectors $\mathbf{A}$ and $\mathbf{B}$ for the restriction to 2D. We assume that the 2D field is defined on the *x-y* plane. For this, the 3D field has to meet two requirements. First, the *z*-component of the flux density has to vanish everywhere, i.e., $B_z \equiv 0$. Second, $\mathbf{B}$ should be independent from the *z*-position, i.e., it should be shift-invariant in *z*-direction.

These requirements lead to two constraints for the vector potential $\mathbf{A}$. First, $\mathbf{A}$ can be modeled as vectors that only have a *z*-component; their *x*- and *y*-components vanish. Second, the vector potential is independent from the *z*-position. With
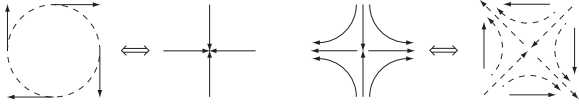
Figure 2: *Centers (left) are converted to sources or sinks (depending on their orientation) under the action of P, since every vector is rotated by $-\frac{\pi}{2}$. Saddles (right) are rotated by $-\frac{\pi}{4}$ under the action of P.*
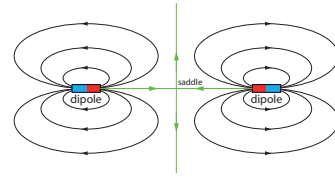

Figure 3: *In such a configuration, there is no magnetic field line that connects the two dipoles. All magnetic field lines are separated by the separatrices (green).*

these constraints, we obtain the magnetic flux density

$$\mathbf{B} = \operatorname{curl} \mathbf{A} = \begin{pmatrix} \frac{\partial A_z}{\partial y} \\ -\frac{\partial A_z}{\partial x} \\ 0 \end{pmatrix} \cong \begin{pmatrix} \frac{\partial A}{\partial y} \\ -\frac{\partial A}{\partial x} \end{pmatrix} = \operatorname{curl}_2 A$$

which indeed is a 2D field. In the above equation, the vector potential is rewritten by just using its z-component, with $A_z =: A$. Furthermore, we have introduced the analog of the curl operator in 2D, curl_2. The effect of curl_2 can be expressed as

$$\mathbf{B} = P\nabla A, \quad P = \begin{pmatrix} 0 & 1 \\ -1 & 0 \end{pmatrix}.$$

Geometrically speaking, curl_2 computes the gradient of the scalar potential A and then rotates the gradient vector by $-\frac{\pi}{2}$. This geometric observation is utilized in our following construction of the magnetic flux topology. $\mathbf{B}$ and ∇A are dual vector fields—in this sense, the traditional topology of $\mathbf{B}$ can be considered as the dual of the traditional topology of ∇A.

To derive the relation between primal and dual topology, we examine the effect of P on the topology of the $\mathbf{B}$ and ∇A fields. Since the magnetic flux density $\mathbf{B}$ is divergence-free, it can only contain centers and saddles (and periodic orbits, which are not of interest to us). In turn, the rotation-free ∇A field can contain only sources, sinks, and saddles. Our first observation is that critical points are not affected by P, i.e., critical points of one field are found at the same location in its dual field because P does not change vector magnitude:

$$||\mathbf{x}|| = \sqrt{x^2 + y^2} = \sqrt{y^2 + (-x)^2} = ||P\mathbf{x}||.$$

We continue our examination of the effect of P with respect to centers, sources, and sinks. These topological constructs are isotropic, i.e., they are rotation-invariant. However, P converts sources with their respective vector field

$$\mathbf{u}(\mathbf{x}) = \begin{pmatrix} a & 0 \\ 0 & a \end{pmatrix} \mathbf{x}, \quad a > 0$$

into counter-clockwise centers with

$$\mathbf{u'}(\mathbf{x}) = P \begin{pmatrix} a & 0 \\ 0 & a \end{pmatrix} \mathbf{x} = \begin{pmatrix} 0 & a \\ -a & 0 \end{pmatrix} \mathbf{x}.$$

Changing the sign of a results in a sink that converts likewise to a clockwise center when applying P. This effect is illustrated on the left side of Fig. 2. As a result, dipoles in $\mathbf{B}$,

which can be interpreted as the composition of centers of opposite orientation at infinitesimally close distance, find their counterpart as infinitesimally close pairs of a source and sink in ∇A. Finally, we examine the effect of P for saddles. As a first step, we show that P does not change the determinant of any matrix M:

$$\det M = \det \begin{pmatrix} a & b \\ c & d \end{pmatrix} = ad - cb$$

$$\det PM = \det \begin{pmatrix} 0 & 1 \\ -1 & 0 \end{pmatrix} \begin{pmatrix} a & b \\ c & d \end{pmatrix} = -cb + ad$$

Since $\det M$ is invariant under P, the condition for saddles of a negative determinant is not affected by P, which means that saddles in one field persist in the dual field. Now, we consider the orientation of a saddle when applying P. For the sake of simplicity, we limit the investigation to axis-aligned saddles,

$$\mathbf{u}(\mathbf{x}) = \begin{pmatrix} -a & 0 \\ 0 & b \end{pmatrix} \mathbf{x}, \quad a, b > 0$$

and apply P:

$$\mathbf{u'}(\mathbf{x}) = P \begin{pmatrix} -a & 0 \\ 0 & b \end{pmatrix} \mathbf{x} = \begin{pmatrix} 0 & b \\ a & 0 \end{pmatrix} \mathbf{x}$$

which results in eigenvalues $\lambda_{1,2} = \pm\sqrt{ab}$ of $\nabla\mathbf{u'}$. The eigenvectors of this saddle compute as:

$$\begin{pmatrix} x \\ \pm\sqrt{\frac{a}{b}}x \end{pmatrix}.$$

Hence, saddles with $a = b$ of one field are rotated by $-\frac{\pi}{4}$ in the dual field, as illustrated on the right side of Fig. 2. For arbitrary values of a, b, the dual saddle is deformed, however, this is not of importance to us.

4. Flux Topology

In this section, we introduce our flux topology that describes if, and how much, flux is present between dipoles.

4.1. Connection Regions

We start our discussion with dipoles that are oriented in opposite direction and create magnetic fields as illustrated in
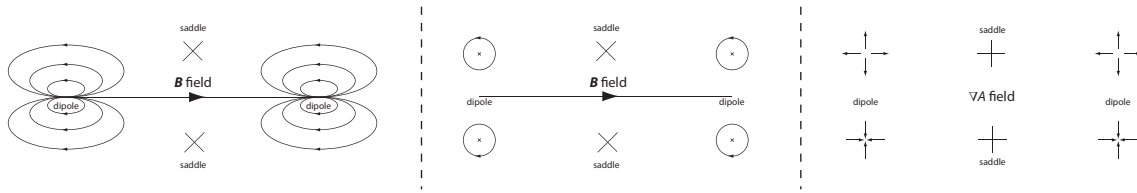
Figure 5: *Left: two dipoles are oriented in the same direction, which results in magnetic flux between both dipoles heading from left to right. Middle: the two centers of a dipole, which are infinitly close together, are shifted apart for illustration purposes only. Right: the two centers of a dipole within **B** are replaced by a source and a sink in the corresponding ∇A field according to the dual topology rules.*

Fig. 3. There is no magnetic field line passing through both dipoles (the separatrices converge to the saddle in infinite time). Changing the configuration to consistent orientation results in a region that is of special interest to us and is illustrated in Fig. 4. This region consists of all magnetic field lines that connect one dipole with the other one, as shown in Fig. 4. We call this region *dipole flux connection region*, or shorter, *connection region*. This region is bounded by the separatrices that start at the two saddles located between the dipoles and run through both dipoles.

The magnetic field lines around a dipole form closed curves with the centers of these curves approaching the dipole center infinitely close. If more than one dipole is involved, some of the field lines can pass through other dipoles, as illustrated in Fig. 5 (left). For the sake of simplicity of illustration, we grow the infinitesimal distance between the two centers of a dipole. Every configuration of two dipoles connected by a magnetic field line can be converted into a topologically equivalent configuration as shown in Fig. 5 (left) and consecutively into the configuration shown in Fig. 5 (middle). The next step is to switch from the **B** field to the dual ∇A field, as shown in Fig. 5 (right). As discussed in Sect. 3.2, the two centers of a dipole are now replaced by a source and a sink. In addition, the two saddles located between the dipoles are rotated (and possibly deformed).

The next step in our reasoning is to consider the field lines of the ∇A field, which are shown in Fig. 6a. Please note that the source and sink pairs represent again dipoles in the ∇A field. In general, i.e., in non-degenerate cases without a

saddle-saddle connection, a Morse-Smale cell forms in ∇A between the original dipoles in **B**. The final step in our reasoning switches back to the **B** field, shown in Fig. 6b. We can see that the Morse-Smale cell of the dual ∇A field converts to our connection region. Hence, we have shown that there is always a connection region between two dipoles that share a magnetic field line. Also, such a connection region will always be defined by the two dipoles and consequently by the two corresponding saddles.

4.2. Connectrices

Once we have found a connection region, we want to visualize the magnetic flux through this region in a topological manner, i.e., we preserve its topology (connectivity of dipoles) and neglect its morphology. To do this, we provide a mathematical definition of connectrices.

We start with the set of all dipoles D. A field line connecting to dipole $d_1 \in D$ either extends to infinity or connects to another dipole $d_2 \in D$, where $d_1 = d_2$ is allowed. Please note that we stop a field line when it reaches a dipole. To proceed, we define $F_{P_{1,2}}$ as the set of all field lines that con-
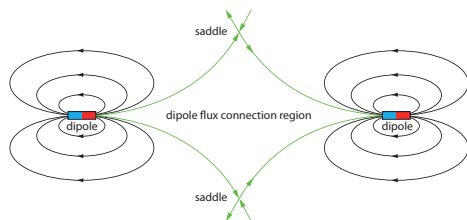

Figure 4: *Dipoles are oriented into the same direction. We call the region delineated by the separatrices (green) a dipole flux connection region.*
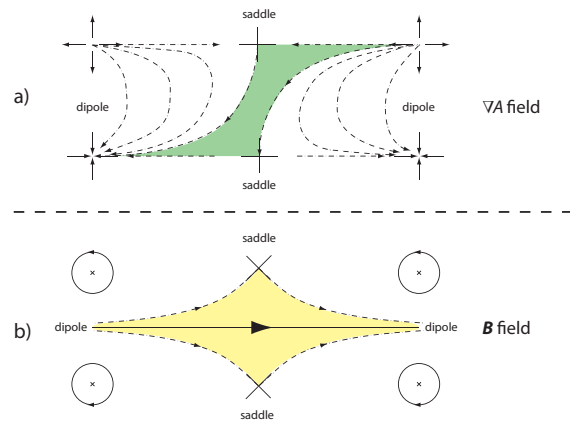

Figure 6: *a) A Morse-Smale cell (green) can be found in the ∇A field between connected dipoles. b) Returning to the **B** field, a respective connection region (yellow) is found between the two dipoles.*
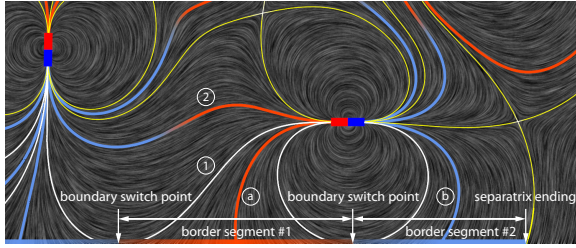
Figure 7: *Boundary flux indicators at the bottom visualize flux affecting dipoles from the outside. Two boundary switch points and a separatrix of **B** form border segments #1 and #2, which in turn give rise to semi-connectrices (a) and (b). The "virtual" separatrix (1) is started at the left boundary switch point and closes the connection region represented by connectrix (2).*

nect to both d_1 and d_2, where $P_{1,2} : \{d_1, d_2\}$ and $d_1 \neq d_2$. $F_{P_{1,2}}$ is the connection region. Now we define two field lines f_i, f_j to be equivalent iff $f_i, f_j \in F_{P_{1,2}}$.

Hence, any one field line $f_i \in F_{P_{1,2}}$ is topologically equivalent to $F_{P_{1,2}}$. We call such a field line f the *dipole connectrix*, or shorter, *connectrix* of the connection region $F_{P_{1,2}}$. In Sect. 5.2, we will show how we obtain a visual representation of a connectrix. The magnetic flux within the connection region is visualized by the thickness of the line representation of the connectrix, and the orientation of the flux using a transition from red (north) to blue (south). The magnetic flux of such a region could be computed by integrating the magnetic flux density along any curve that connects the separatrices of the two respective saddles and stays within the connection region. As we will see in Sect. 5.3, we can avoid such an integration process and use a much simpler approach to compute the magnetic flux.

4.3. Complete Topology

Our method supports domains with boundaries, e.g., limited rectangular domains that might serve as a window or come from simulations with boundaries. Within such a domain, we search for saddle-type critical points using a sampling grid. Please note that critical point extraction is the only step in our approach where a discretized version of the field is required. The remaining process can act solely on the original data given as a set of point dipoles.

If a saddle is located outside of our sampling grid, we cannot take it into account for detecting connection regions. Therefore, a connection region that would be defined by such a saddle is not found, which would lead to missing connectrices. We address this problem by introducing boundary flux indicators that visualize where, and how much, flux crosses the borders of the data set or the boundary of the sampling grid. Boundary flux indicators are constructed as follows: to begin, we locate boundary switch points [WTHS04] of

B, i.e., points where **B** is tangential to the boundary. In our case, these points represent extrema of A along the boundary, which allows a simplified extraction by scanning the vector potential A of the outermost cells of our sampling grid. The boundary switch points serve two purposes: First, they adopt the role of saddles when extracting connection regions—they are starting points for "virtual separatrices" in **B**, which are constructed only to delimit a connection region that would otherwise be left open (e.g., connectrix (2) in Fig. 7 would be missing). Second, they form a set S_{bsp}, whereas end points of separatrices in **B** that leave the sampling grid form a set S_{s}. These two sets form $S = S_{\text{s}} \cup S_{\text{bsp}}$. For two adjacent elements $e_{1,2} \in S$, we create a border segment, i.e., a segment on the boundary of the sampling grid delimited by e_1 and e_2. For each border segment, we construct "semi-connectrices"—connectrices that are attached only to one dipole and end at their corresponding border segment. A semi-connectrix is colored depending on the pole of the dipole to which it connects.

As for regular connectrices, we will see in Sect. 5.3 that we can use a similarly simple approach to compute the corresponding flux. In addition, we visualize the border segments using boundary flux indicators: bars of fixed width that span the border segment and are of the same color as the corresponding semi-connectrix.

In total, there are three different kinds of boundary indicators depending on the type of $e \in S$ that delimits the border segment: $e_{1,2} \in S_{\text{s}}$, $e_1 \in S_{\text{s}}$ and $e_2 \in S_{\text{bsp}}$, and $e_{1,2} \in S_{\text{bsp}}$. If $e \in S_{\text{bsp}}$, we apply gradual transparency at e. This indicates that the corresponding semi-connectrix visualizes flux together with the connectrix of the adjacent connection region. If $e \in S_{\text{s}}$, full opacity is used instead. Fig. 7 illustrates this situation.

5. Connectrix Algorithm

The algorithm that constructs connectrices is split in two parts. The first step (Sect. 5.1) finds all connection regions in the data set. In the second step (Sect. 5.2), one connectrix is created for each connection region.

5.1. Finding Connection Regions

To find connection regions, we have to detect all saddles as well as corresponding separatrices in the magnetic field. Separatrices are started at saddles and traced until they end at a dipole or leave the sampling grid. Depending on which pole of a dipole is hit by the separatrix, we define the separatrix to be of type "north" or "south".

Once all separatrices of the **B** field are created, we have the necessary data to identify connection regions. These regions are defined by two dipoles, two corresponding saddles, and are bounded by the separatrices that connect them as illustrated in Fig. 4. Separatrices ending at the first dipole have
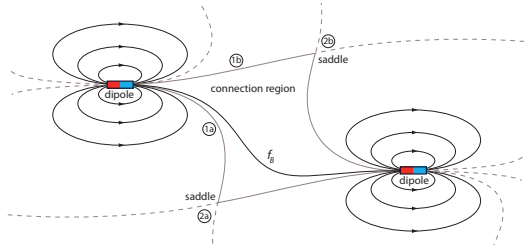
Figure 8: *Identifying connection regions: start with neighboring separatrices* ①ₐ *and* ①ᵦ *of the left dipole along with saddles at* ②ₐ *and* ②ᵦ. *To identify the second dipole, follow a field line* f_B *in* **B** *starting at the left dipole.*

Figure 9: *Constructing a connectrix: field line tracing is performed along* ∇A *into the same direction as the halfway vector* **h** *at* ① *until* a_{avg} *is found in A at* ②. *Tracing forwards and backwards in* **B** *constructs the connectrix for this connection region.*

to be of opposite type (either "north" or "south") than the two separatrices ending at the second dipole. If the dipoles are facing each other in a topologically equivalent configuration (as shown in Fig. 3), a connectrix cannot exist. In addition, we do not allow self-connectrices, i.e., connectrices that start and end at the same dipole.

This all leads to the algorithm described below. As a preliminary step, we sort all separatrices at a dipole that are of the same type (either "north" or "south") according to the potential A. The potential of a separatrix is obtained from the corresponding saddle position. This sorting allows us to choose "neighboring" separatrices with respect to the potential, which is essential to the algorithm.

1. For each dipole d, consider only separatrices of type "north", which form the set S_d.
2. Follow all pairs of neighboring separatrices $s_{1,2} \in S_d$; check that $s_{1,2}$ connect to different saddles.
3. Start a field line f_B in **B** at d between $s_{1,2}$ and trace away from d (backward if necessary) until a dipole d' is reached.
4. A connection region is found iff $d' \neq d$.
5. Obtain separatrices of type "south" of d accordingly.

This first part of our approach is depicted in Fig. 8 with a representative example scene. Please note that the field line f_B is already a valid connectrix according to our definition. However, in order to create a good representation of the connectrix, we perform the additional steps described in the following section.

5.2. Constructing Connectrices

The second part of our method constructs a representative connectrix for each connection region. The main task is to find an appropriate seed point within this region that generates the connectrix by field line integration in **B** in both directions until both dipoles are reached. The idea is to choose the field line that corresponds to the mean value of the potential A of the respective connection region—in the sense of a "mean" position. We propose the following approach to
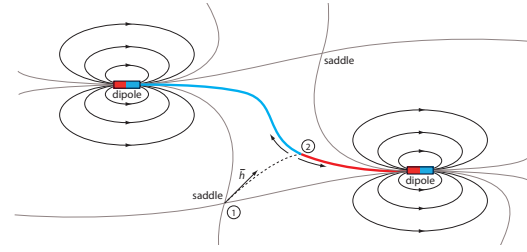
find a seed point (a special case of numerical root finding) and to construct a connectrix, as illustrated in Fig. 9.

1. Evaluate A at the two saddle positions and compute the average a_{avg}. This represents the mean potential within the connection region.
2. Choose one of the two saddles arbitrarily and perform field line tracing in the ∇A field, heading into the connection region. Please note that this is not immediately possible, since $\nabla A = 0$ at a saddle position. Therefore, follow the half-way vector of the two separatrices that meet at the chosen saddle position. We use a small step, typically $1/10^{\text{th}}$ of the cell size of the sampling grid. Perform field line tracing in ∇A to advance inside the connection region.
3. At each step of the tracing process in the ∇A field, access the value of A at the current tracing location. Once the value of the A field crosses the average value a_{avg}, the seed point for the connectrix is found by bisection.
4. From that point, perform forward and backward integration in **B** until a dipole is reached, yielding the connectrix.

In step 2, one can choose between the two saddles of the connection region as a starting point for the tracing process in the ∇A field. The resulting seed points for the connectrix are different depending on the chosen saddle; however, both seed points will be located on the same fieldline of the **B** field due to the duality of the ∇A and **B** fields and because of a unique a_{avg}. This is due to the fact that A is a stream function for **B**, i.e., contours in A represent field lines in **B**. Please note that therefore the final visualization for the connectrix is independent of the chosen saddle point.

5.3. Visualizing Magnetic Flux

In addition to encoding the topology of the flux between dipoles, we visualize the flux magnitude by varying the line width of the connectrices. This emphasizes connectrices of dipoles that create a strong magnetic flux.

The magnetic flux through a connection region is defined as the integral of the magnetic flux density **B** along any curve

within this region that connects the separatrices of the two saddles. However, we can avoid this integration: we just have to evaluate *A* at the two saddle locations. The difference of these two potentials equals the magnetic flux through the connection region. Since the potential *A* works analogous to a stream function, integration of flux over a curve can be replaced by a difference in the potentials of its end points.

5.4. Implementation

Our implementation uses a uniform grid to resample the *A* and **B** fields defined by the given set of dipoles. Critical points are detected according to the approach described in [HH91]. Both separatrices and connectrices are constructed using field line integration that is performed using an adaptive step-size, fourth-order Runge-Kutta algorithm. We stop the integration process when entering a cell that contains a dipole or when leaving the sample grid. Therefore, we choose our sampling grid so that cells are small enough to contain at most one dipole.

We implemented our prototype in C# using the Microsoft XNA [MS] framework on a system with an Intel Core i7 CPU running at 3.4 GHz and an NVIDIA GeForce 580 GPU. Magnetic field lines are visualized with an HLSL-Shader implementation of line integral convolution [CL93].

6. Application

To demonstrate the utility of our method, we apply it to simulations from the domain of soft-matter sciences [KCH08]. All data sets are initially represented as collections of dipoles with varying position, orientation, and magnitude of magnetic moment. To improve the visibility of the topological structures, we omit the LIC-visualization of the **B** field.

6.1. Monolayer

In Fig. 10, we present a snapshot obtained for a ferroparticle monolayer consisting of 128 dipoles. In this case, the interparticle interaction is strong enough for the magnetic particles to form various small clusters. The prevalent topological structures in our visualization of the magnetic flux are chains and rings, readily classifying the clusters into these two groups (see, e.g., center of Fig. 10). Moreover, our visualization gives quantitative insight in their magnetic properties, e.g., distinguished chains and loops in the visualization represent clusters with strong magnetic interaction. In this way, our technique provides a powerful approach to the analysis of ferroparticle monolayers, e.g., to differentiate between randomly aligned particles and stable clusters. This is of particular importance for understanding the microstructure of ferrofluids in confinement.

6.2. Ferrogel

With the series of images shown in Fig. 11 and Fig. 12, we present the time evolution spanning 1 000 time steps of a
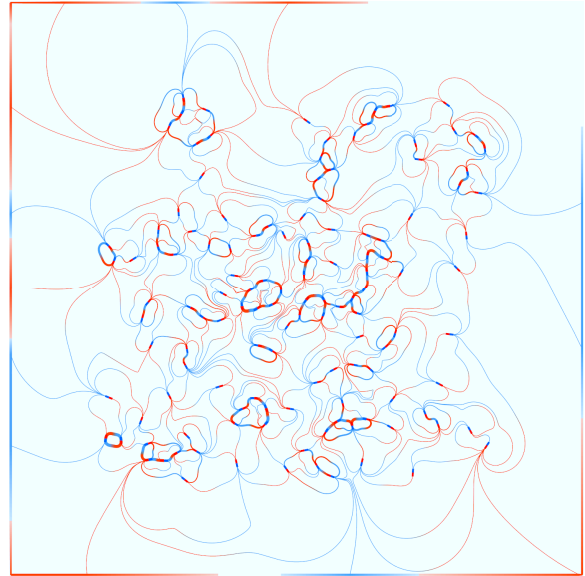

Figure 10: *Monolayer data set. Ring and chain structures can be readily identified in our flux topology visualization. Computing the flux topology takes 14.74 seconds.*

magnetic gel simulation. The gel with an initially square lattice (connectivity indicated by black lines) composed of 4 104 dipoles and additional non-magnetic particles (visualized as black dots) is exposed to a strong external magnetic field which is aligned from left to right in the images. As the properties of the gel primarily depend on dipole–dipole interaction, we omit this external field in our visualizations.

In the first snapshot, one can still see the signature of a square lattice. Here, lattice segments that are aligned with the external field are part of chains of pronounced magnetic flux. In contrast, particles on segments perpendicular to the field are rarely part of a common connectrix. They are rather part of long, weak connectrices between neighboring lattice segments, or part of weak loop-like structures. The overall shape of the magnetic ferrogel still reflects the initial lattice because the strong horizontal chains have a repulsive effect on each other. The formation of horizontal connectrix chains proceeds during the later time steps. As these structures grow in strength of magnetic flux, the ferrogel is locally contracted, displacing the non-magnetic particles into saw-tooth shaped configurations. At the same time, the overall shape of the gel sample undergoes a transition into diamond-shaped configuration, as the dipoles with energetically less advantageous configuration rearrange. In the final snapshot, the majority of the lattice segments assume a diagonal orientation, with long chains of dipoles that are maximally coaligned with the external magnetic field.
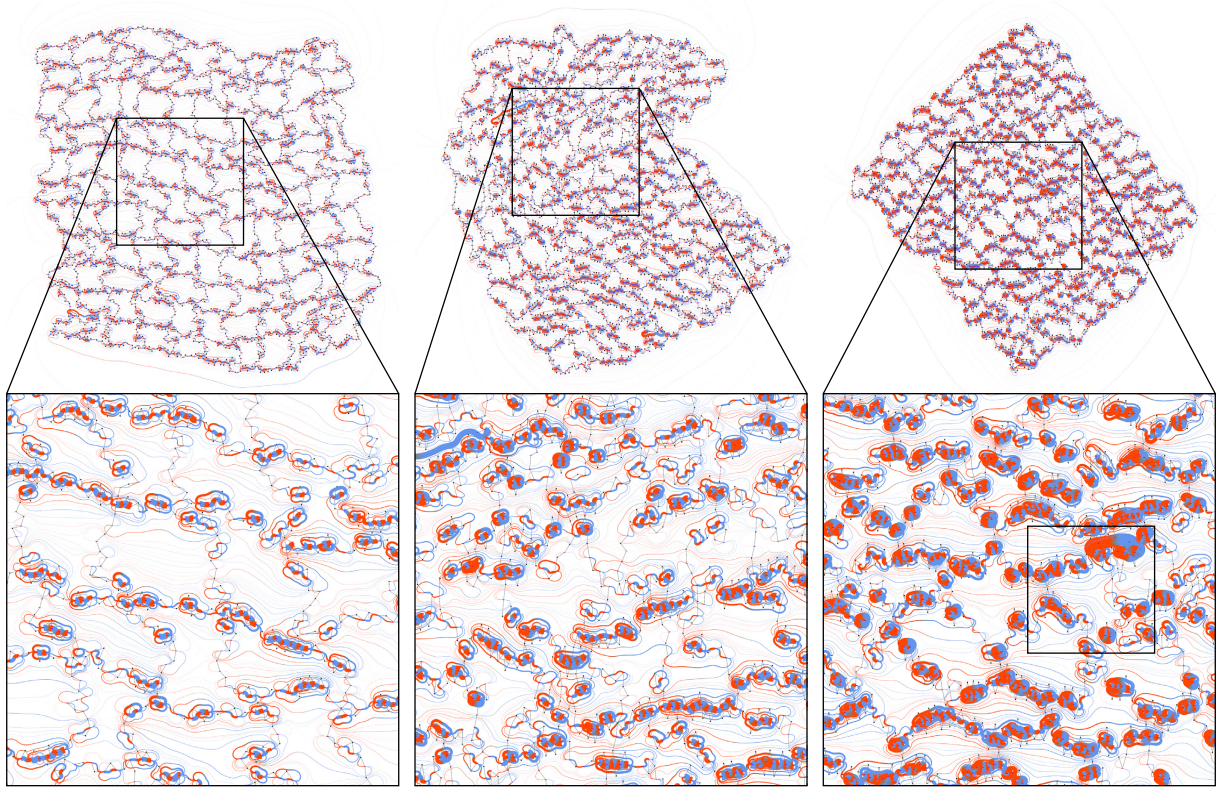
Figure 11: *From left to right: time steps 1, 500, and 900 of a ferrogel simulation. Upper row: whole data set; lower row: zoomed-in views of the regions denoted by black rectangles. For all images, the same scaling for the flux magnitude was used. Non-magnetic particles are shown as black dots. Computing the flux topology takes 256, 270, and 264 seconds, respectively.*

7. Conclusion

We have presented magnetic flux topology to reveal the global structure of magnetic fields induced by dipoles. Compared to topological methods based on separatrices, our technique additionally provides a quantitative picture because it represents transport regions instead of separating regions. For complex data sets, this compact visual representation allows us to reduce visual clutter and overall complexity of the resulting visualization. The applications from soft-matter sciences have shown that the connectrix structure is well aligned with other structural elements of materials, allowing the user to analyze the simulation of magnetic material by magnetic flux topology.

An open question left for future work is the extension to three dimensions. The main challenge is that the scalar-valued potential A will have to be extended to a 3-component vector field potential.
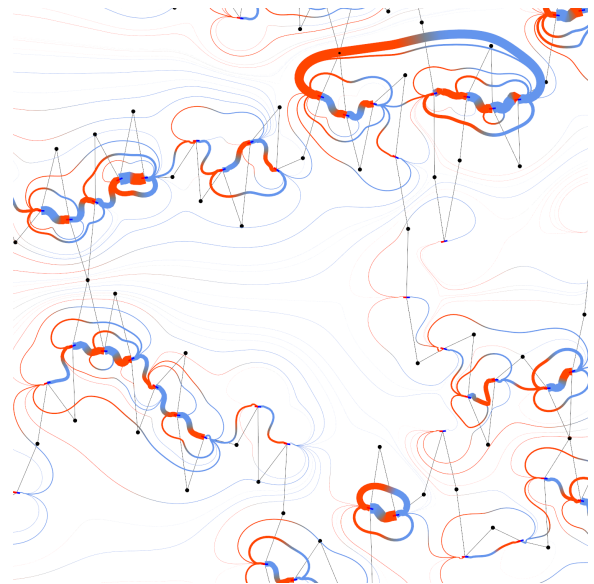
Figure 12: *This view corresponds to the black rectangle in the lower right image of Fig. 11. Flux is scaled down by one order of magnitude to reduce visual clutter.*

References

[ABB*11] ANDRAE D., BARTH I., BREDTMANN T., HEGE H.-C., MANZ J., MARQUARDT F., PAULUS B.: Electronic quantum fluxes during pericyclic reactions exemplified for the cope rearrangement of semibullvalene. *The Journal of Physical Chemistry B 115*, 18 (2011), 5476–5483. 3

[BHI*09] BARTH I., HEGE H.-C., IKEDA H., KENFACK A., KOPPITZ M., MANZ J., MARQUARDT F., PARAMONOV G. K.: Concerted quantum effects of electronic and nuclear fluxes in molecules. *Chemical Physics Letters 481*, 1-3 (2009), 118–123. 3

[BW08] BACHTHALER S., WEISKOPF D.: Animation of orthogonal texture patterns for vector field visualization. *IEEE Transactions on Visualization and Computer Graphics 14*, 4 (2008), 741–755. 3

[CL93] CABRAL B., LEEDOM L. C.: Imaging vector fields using line integral convolution. In *Proc. of the ACM SIGGRAPH 1993 Conference* (1993), pp. 263–270. 8

[CLN05] CAI D., LEMBEGE B., NISHIKAWA K.: Visualizing magnetospheric vector field topology. In *Proc. of ISSS-7* (2005), pp. 26–31. 2

[GBHP08] GYULASSY A., BREMER P.-T., HAMANN B., PASCUCCI V.: A practical approach to Morse-Smale complex computation: Scalability and generality. *Visualization and Computer Graphics, IEEE Transactions on 14*, 6 (2008), 1619–1626. 2

[HH89] HELMAN J., HESSELINK L.: Representation and display of vector field topology in fluid flow data sets. *Computer 22*, 8 (1989), 27–36. 2

[HH91] HELMAN J., HESSELINK L.: Visualizing vector field topology in fluid flows. *IEEE Computer Graphics and Applications 11*, 3 (1991), 36–46. 2, 8

[Jac75] JACKSON J. D.: *Classical Electrodynamics*, 2nd ed. Wiley, New York, NY, 1975. 3

[KCH08] KANTOROVICH S., CERDA J. J., HOLM C.: Microstructure analysis of monodisperse ferrofluid monolayers: theory and simulation. *Physical Chemistry Chemical Physics 10* (2008), 1883–1895. 2, 8

[KDK*06] KLOKKENBURG M., DULLENS R. P. A., KEGEL W. K., ERNÉ B. H., PHILIPSE A. P.: Quantitative real-space analysis of self-assembled structures of magnetic dipolar colloids. *Physical Review Letters 96* (2006), 037203. 2

[KE04] KLEIN T., ERTL T.: Illustrating magnetic field lines using a discrete particle model. In *Workshop on Vision, Modelling, and Visualization VMV '04* (2004), pp. 387–394. 2

[LHZP07] LARAMEE R., HAUSER H., ZHAO L., POST F.: Topology-based flow visualization, the state of the art. In *Topology-Based Methods in Visualization (Proc. of Topology-Based Methods in Visualization 2005)* (2007), pp. 1–19. 2

[LLC*11] LIPŞA D. R., LARAMEE R. S., COX S. J., ROBERTS J. C., WALKER R.: Visualization for the physical sciences. In *Eurographics* (2011). State-of-the-Art Reports. 3

[MS] Microsoft XNA framework. `http://create.msdn.com`. (last accessed 01.03.2012). 8

[PDKH09] PROKOPIEVA T. A., DANILOV V. A., KANTOROVICH S. S., HOLM C.: Ground state structures in ferrofluid monolayers. *Physical Review E 80* (2009), 031404. 2

[PS07] PEIKERT R., SADLO F.: Visualization methods for vortex rings and vortex breakdown bubbles. In *Proc. of the Joint Eurographics - IEEE VGTC Symposium on Visualization (EuroVis 2007)* (2007), pp. 211–218. 2

[PS09] PEIKERT R., SADLO F.: Flow topology beyond skeletons: Visualization of features in recirculating flow. In *Topology-Based Methods in Visualization II* (2009), Springer, pp. 145–160. 2

[RDT*10] REINICKE S., DOHLER S., TEA S., KREKHOVA M., MESSING R., SCHMIDT A. M., SCHMALZ H.: Magneto-responsive hydrogels based on maghemite/triblock terpolymer hybrid micelles. *Soft Matter 6* (2010), 2760–2773. 2

[RPP*09] ROSANWO O., PETZ C., PROHASKA S., HOTZ I., HEGE H.-C.: Dual streamline seeding. In *Proc. of IEEE PacificVis '09* (2009), pp. 9–16. 3

[SCT*10] SANDERSON A., CHEN G., TRICOCHE X., PUGMIRE D., KRUGER S., BRESLAU J.: Analysis of recurrent patterns in toroidal magnetic fields. *IEEE Transactions on Visualization and Computer Graphics 16* (2010), 1431–1440. 2

[SCTC11] SANDERSON A., CHEN G., TRICOCHE X., COHEN E.: Understanding quasi-periodic fieldlines and their topology in toroidal magnetic fields. *Accepted at Topological Methods in Data Analysis and Visualization II—Theory, Algorithms, and Applications* (2011). 2

[SHK*97] SCHEUERMANN G., HAGEN H., KRÜGER H., MENZEL M., ROCKWOOD A. P.: Visualization of higher order singularities in vector fields. In *Proc. of IEEE Visualization* (1997), pp. 67–74. 2

[SPP04] SADLO F., PEIKERT R., PARKINSON E.: Vorticity based flow analysis and visualization for pelton turbine design optimization. In *IEEE Visualization* (2004), pp. 179–186. 2

[SPS06] SADLO F., PEIKERT R., SICK M.: Visualization tools for vorticity transport analysis in incompressible flow. *IEEE Transactions on Visualization Computer Graphics 12*, 5 (2006), 949–956. 2

[SRB11] STOLBOV O. V., RAIKHER Y. L., BALASOIU M.: Modelling of magnetodipolar striction in soft magnetic elastomers. *Soft Matter 7* (2011), 8484–8487. 2

[Sun03] SUNDQUIST A.: Dynamic line integral convolution for visualizing streamline evolution. *IEEE Transactions on Visualization and Computer Graphics 9, 3* (2003), 273–282. 2

[TGPS08] THOMASZEWSKI B., GUMANN A., PABST S., STRASSER W.: Magnets in motion. *ACM Transactions on Graphics 27*, 5 (2008), 162:1–162:9. 2

[WC11] WOOD D. S., CAMP P. J.: Modeling the properties of ferrogels in uniform magnetic fields. *Physical Review E 83* (2011), 011402. 2

[WS01] WISCHGOLL T., SCHEUERMANN G.: Detection and visualization of closed streamlines in planar flows. *IEEE Transactions on Visualization and Computer Graphics 7, 2* (2001), 165–172. 3

[WTHS04] WEINKAUF T., THEISEL H., HEGE H.-C., SEIDEL H.-P.: Boundary switch connectors for topological visualization of complex 3D vector fields. In *Proc. Joint Eurographics - IEEE TCVG Symposium on Visualization (VisSym '04)* (2004), pp. 183–192. 6

[Zri00] ZRINYI M.: Intelligent polymer gels controlled by magnetic fields. *Colloid & Polymer Science 278* (2000), 98–103. 2